

Article

Development of Refractory High Entropy Alloys with Tensile Ductility at Room Temperature

Zhangquan Liu ¹, Xiaohui Shi ¹, Min Zhang ¹ and Junwei Qiao ^{1,2,*}¹ College of Materials Science and Engineering, Taiyuan University of Technology, Taiyuan 030024, China² Key Laboratory of Interface Science and Engineering in Advanced Materials, Ministry of Education, Taiyuan University of Technology, Taiyuan 030024, China

* Correspondence: qiaojunwei@gmail.com

Abstract: In this study, a low-cost refractory high-entropy alloy (RHEA) with obvious macroscopic tensile ductility was designed. The evolution of the microstructures and fundamental mechanical properties with the TiZr concentration in arc-melted $(\text{TiZr})_x(\text{NbTaV})_{1-x}$ ($x = 0.4, 0.6,$ and 0.8) high-entropy alloys (HEAs) were investigated. The alloys $(\text{TiZr})_{0.4}(\text{NbTaV})_{0.6}$ and $(\text{TiZr})_{0.6}(\text{NbTaV})_{0.4}$ had a single body-centered cubic solid solution phase. Two phases were confirmed in the as-cast $(\text{TiZr})_{0.8}(\text{NbTaV})_{0.2}$ alloy using X-ray diffraction and scanning electron microscopy. All three alloys had dendritic structures with severe element segregation. $(\text{TiZr})_{0.4}(\text{NbTaV})_{0.6}$ had a high yield strength of 1300 MPa with a compressive fracture strain of 16%. $(\text{TiZr})_{0.8}(\text{NbTaV})_{0.2}$ showed exceptional compressive plasticity but a low yield strength. $(\text{TiZr})_{0.6}(\text{NbTaV})_{0.4}$ had a relatively uniform yield strength and compressive fracture plasticity (950 MPa and 35%). In addition, $(\text{TiZr})_{0.8}(\text{NbTaV})_{0.2}$ also had a tensile ductility of 7% at room temperature.

Keywords: high-entropy alloys; refractory; design; multiphase; tensile plasticity

Citation: Liu, Z.; Shi, X.; Zhang, M.; Qiao, J. Development of Refractory High Entropy Alloys with Tensile Ductility at Room Temperature. *Metals* **2023**, *13*, 329. <https://doi.org/10.3390/met13020329>

Academic Editor: Babak Shalchi Amirkhiz

Received: 11 January 2023

Revised: 29 January 2023

Accepted: 1 February 2023

Published: 6 February 2023



Copyright: © 2023 by the authors. Licensee MDPI, Basel, Switzerland. This article is an open access article distributed under the terms and conditions of the Creative Commons Attribution (CC BY) license (<https://creativecommons.org/licenses/by/4.0/>).

1. Introduction

With the advancement of modern industry, high-performance materials with high strength, ductility, and thermal stability are in high demand in a variety of applications [1]. Conventional alloys are composed of one main element and a few minor alloying elements to improve the mechanical characteristics of the materials. Over the past decade, a new alloy design and optimization philosophy called multiprincipal-element or high-entropy alloys (HEAs) have drawn increasing attention [2,3]. Generally speaking, such kinds of alloys have five or more elements with equimolar or near-equimolar ratios, but now, the definition of HEAs is more extensive, i.e., composing of at least five major elements, each with an atomic percentage (at.%) between 5% and 35%. It is worth mentioning that the atomic percentage of each minor element, if any, is even smaller than 5% [4]. In HEAs, the low Gibbs free energy caused by high configurational entropy ensures the formation of simple solid solutions rather than intermetallics, usually including typical face-centered cubic (FCC) [2], body-centered cubic (BCC) [5], and hexagonal close-packed (HCP) [6]. Specifically, some BCC HEAs have shown unusual properties, such as high phase stability at elevated temperatures [7]. Up to now, commonly developed Ni-based superalloys can not meet the demands of the fast-growing aerospace industry. New kinds of refractory metals and alloys that have higher melting points are badly needed as alternatives. However, refractory metallic materials face two main problems: low ductility for easy processing at room temperature and poor oxidation resistance at elevated temperatures [8]. Combining the concepts of high entropy and refractory alloys, refractory high-entropy alloys (RHEAs) have been designed to solve these problems. Because high configurational entropy usually leads to high-temperature stability with low Gibbs free energy at high temperatures, this would be one of the advantages of RHEAs [5]. Although

many RHEAs show high compressive strength and large plasticity at ambient temperatures, tensile ductility has not often been achieved in the developed RHEAs up to now [9].

At present, there are two kinds of RHEAs with tensile ductility; one is the single-phase BCC NbTaHfZrTi alloy, with tensile ductility close to 10% after cold rolling and heat treatment [10]. It is a classical refractory high-entropy alloy and one of the components that have been studied extensively at present. The excellent tensile properties of this alloy can be attributed to the excellent ductility of Hf. The other is the $Ta_xHfZrTi$ series alloy. All alloys of this series have good room-temperature tensile ductility, and the tensile ductility of the $Ta_{0.5}HfZrTi$ alloy reaches 30% [11]. These alloys adopt the metastable design concept of titanium alloys. By reducing the content of the Ta element, new phases appear in the alloy so as to improve the mechanical properties of the alloy.

The elements used in $Ta_xHfZrTi$ series alloys are high-cost, and this is very disadvantageous to the application prospect of the alloys. To alleviate this problem, here, we tried to replace the most expensive Hf element with the V element of the same subfamily. Another disadvantage is that the yield strength of these alloys is relatively low. Our ultimate goal was to develop a novel RHEA with high strength and toughness at room temperature.

In this work, we tried to adapt a similar strategy to the $TaNbVZrTi$ RHEA to increase its toughness. The content of (TiZr) was gradually increased with the formation of the secondary phase in the HEA system $(TiZr)_x(NbTaV)_{1-x}$. The ultimate goal was to design a relatively inexpensive RHEA with room-temperature tensile ductility. Furthermore, solid solution strengthening (SSS) is significant in strengthening a wide range of alloys, including HEAs, and contributes to increased yield strength in HEAs. Therefore, we also investigated the role of solution strengthening in this series of alloys.

2. Materials and Methods

By vacuum arc melting in a Ti-gettered argon atmosphere, the alloys $(TiZr)_x(NbTaV)_{1-x}$ ($x = 0.4, 0.6, \text{ and } 0.8$) (compositions in at.%) were created. The weight percentage purity of the pure metals was higher than 99.9%. To achieve a homogeneous distribution of elements in the alloys, all ingots were remelted at least five times. Each ingot had a weight of about 30 g. The crystal structures of the as-cast ingots were characterized by an X-ray diffractometer (XRD) using Cu K-alpha radiation through the 2θ range between 20° and 80° , and the scanning rates were $9^\circ/\text{min}$ in all tests. The XRD equipment model is Aeris (PANalytical B.V., Alemlo, The Netherlands). Using a scanning electron microscope (SEM) equipped with a backscatter electron (BSE) mode, we investigated the microstructures and structural evolution of the as-cast $(TiZr)_x(NbTaV)_{1-x}$ alloys. The distribution of elements in all samples was further studied by energy dispersive spectroscopy (EDS). The SEM and EDS tests used the same equipment, model is PhenomWorld (Phenom, Eindhoven, The Netherlands).

For compression tests, as-cast ingots were cut into cylindrical specimens. Each sample measured 3 mm in diameter and 6 mm in height. At room temperature, the compression samples were tested at a strain rate of $5 \times 10^{-4} \text{ s}^{-1}$. For tensile tests, the ingots were cut into slabs with a thickness of 2 mm, cold-rolled to a final thickness of 1.6 mm, and then subjected to 10 min of stress-relief annealing at 1237 K. Then, the specimens for the tensile tests were cut into dog-bone shapes from the slabs and as-cast ingots by electrical discharge machining. The tensile samples had gauge lengths and widths of 15 and 5 mm, respectively. Tensile tests were performed at room temperature using an Instron 5969 universal testing machine. At least five tensile tests were performed on each alloy.

3. Results

3.1. Phases

Figure 1 shows the XRD patterns of the as-cast ingots of $(TiZr)_x(NbTaV)_{1-x}$ RHEAs ($x = 0.4, 0.6, \text{ and } 0.8$). The XRD diffraction peaks of the $(TiZr)_{0.4}(NbTaV)_{0.6}$ alloy were represented by a single BCC phase. As the TiZr content was increased to 0.6, with a composition of $(TiZr)_{0.6}(NbTaV)_{0.4}$, the structure was still single-phase BCC. By contrast,

when the content increased to 0.8, the $(\text{TiZr})_{0.8}(\text{NbTaV})_{0.2}$ alloy had a BCC phase, but a new secondary phase appeared. The secondary phase was preliminarily determined as an HCP phase.

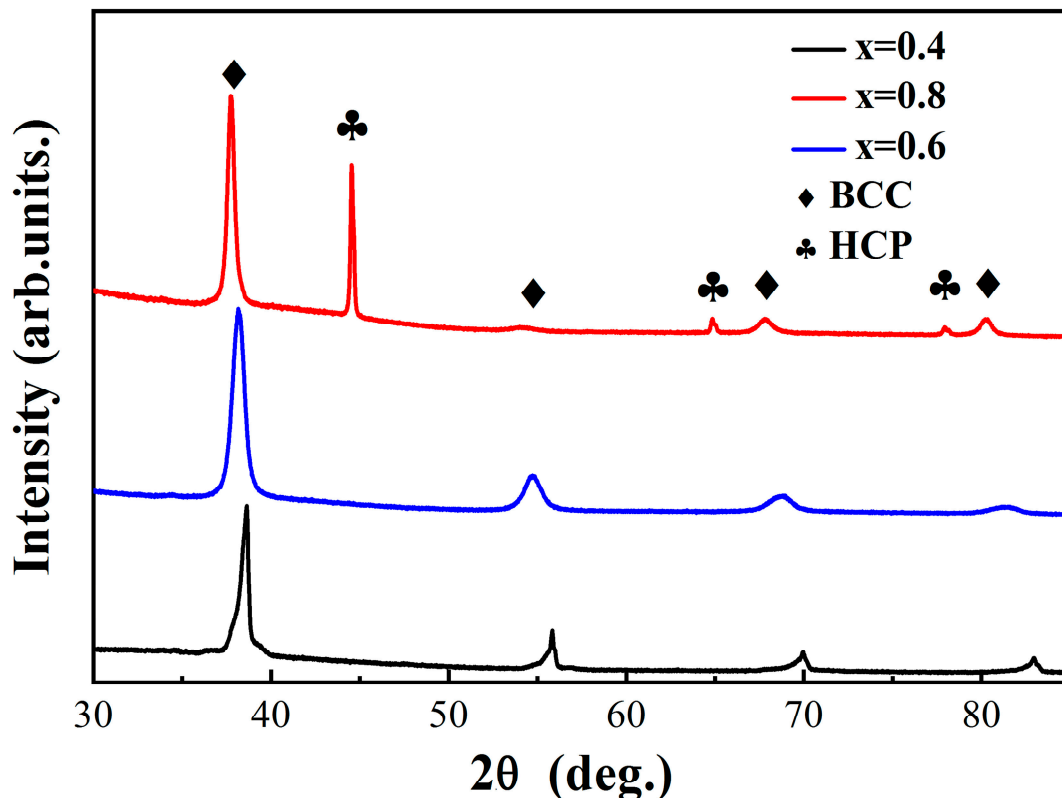


Figure 1. X-ray diffraction patterns of as-solidified HEAs with the compositions of $(\text{TiZr})_x(\text{NbTaV})_{1-x}$ ($x = 0.4, 0.6, \text{ and } 0.8$).

The volume fraction of the secondary phase was quite large in terms of the intensity of the diffraction peak, which will be discussed later. The volume fraction of the BCC phase was determined using the following equation for a material comprising dual phases, such as quenched carbon steel [12]:

$$V_{BCC} = \frac{I_{BCC}/R_{BCC}}{I_{BCC}/R_{BCC} + I_{HCP}/R_{HCP}} \quad (1)$$

Here, I is the X-ray diffraction intensity.

$$R = \left(\frac{m}{v^2} \right) |F|^2 L P e^{-2m} \quad (2)$$

where P is the polarization factor, F is the structure factor, v is the volume of a unit cell, m is the multiplicity factor, and L is the Lorentz factor. All the specific data can be obtained from the literature [12,13]. After calculation, the volume fraction of BCC and HCP phases were 64% and 36%, respectively.

3.2. Microstructures

Figure 2 indicates the backscattered electron SEM images of the $(\text{TiZr})_x(\text{NbTaV})_{1-x}$ RHEAs. Just like typical as-cast ingots, all alloys exhibited a clearly dendritic microstructure. At the same time, a few dark spots could be observed from the dendritic and interdendritic regions in all these alloys. These spots were associated with casting defects. The formation of dendrite structures indicates element segregation. The dendritic space of the three alloys

was not significantly different, which was due to the similar cooling rates during the arc-melting solidification. The bright areas are dendrite arms, and the interdendritic regions appear to be dark on the SEM images. The brightness of the backscattered image depends on the atomic number, and the higher the atomic number, the higher the brightness of the image. This means that the elements with more electrons (such as Nb and Ta) were enriched in the dendrite arms. On the contrary, the elements such as Ti and V, which have smaller atomic numbers, were mainly distributed in inter-dendritic regions. The above situation is supported by many previously reported RHEAs, such as HfNbTaTiZr [10], NbTaTiV [14], and HfNbTiZr [15] RHEAs.

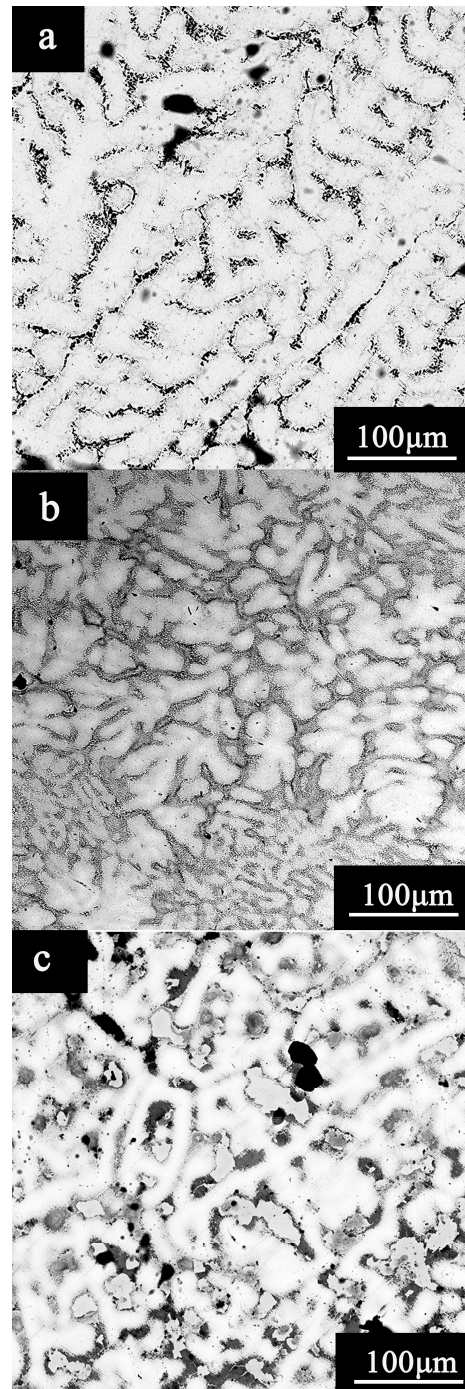


Figure 2. Back-scattered electron SEM images of polished cross-sections of HEAs: (a) $(\text{TiZr})_{0.4}(\text{NbTaV})_{0.6}$, (b) $(\text{TiZr})_{0.6}(\text{NbTaV})_{0.4}$, and (c) $(\text{TiZr})_{0.8}(\text{NbTaV})_{0.2}$.

In order to show the element segregation directly, the energy spectra of each element in the alloy were analyzed by scanning electron microscopy. At the same time, point scanning and surface scanning of the alloys was performed to quantitatively analyze the degree of segregation.

Figure 3a is the energy spectrum of the electron backscatter image and the distribution of each element in the alloys. It can be seen in the figure that the electronic signals of the Ta and Nb elements were dense in the dendrite arm area, and the image was bright, indicating that the element was mainly concentrated in the dendrite arm. By contrast, Zr was primarily abundant in the dendritic area. Finally, the Ti and V elements had no specific tendency and were relatively evenly distributed in the alloys. The element distribution of the $(\text{TiZr})_{0.6}(\text{NbTaV})_{0.4}$ RHEA was similar to that of the $(\text{TiZr})_{0.4}(\text{NbTaV})_{0.6}$ RHEA, while for the $(\text{TiZr})_{0.8}(\text{NbTaV})_{0.2}$ RHEA, the distribution of elements was changed, i.e., Ti and Ta were mostly found in the dendrite arm areas, whereas Nb and V enrichments were seen in the interdendritic regions (see Figure 3b for details). In addition, Zr was mainly concentrated in the secondary phase precipitation, and Ti and Nb were also distributed in large quantities.

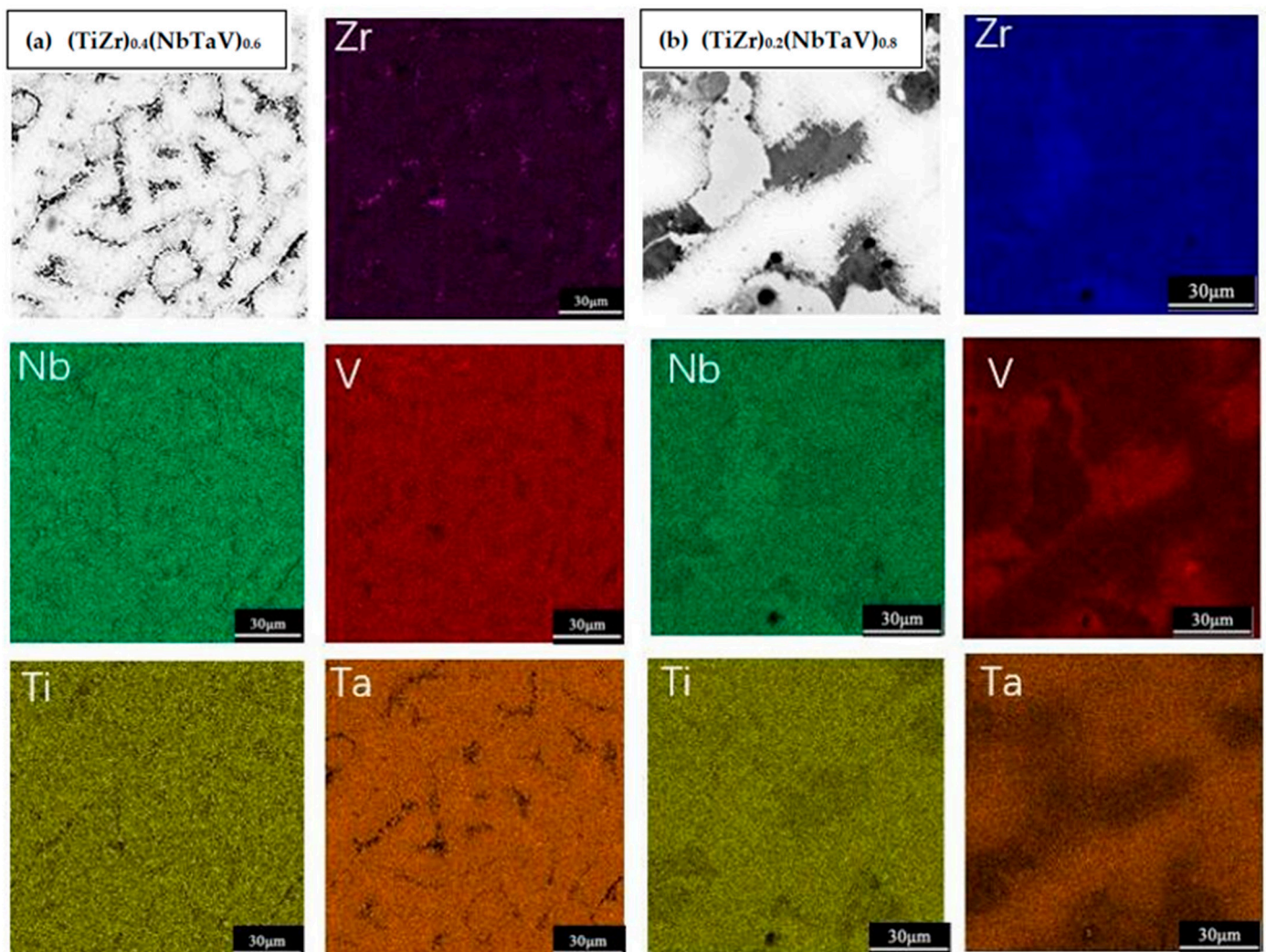


Figure 3. SEM and EDS mapping of Zr, Nb, Ti, V, and Ta in as-cast HEAs: (a) $(\text{TiZr})_{0.4}(\text{NbTaV})_{0.6}$ and (b) $(\text{TiZr})_{0.8}(\text{NbTaV})_{0.2}$.

Table 1 lists the average composition of each element, the composition in the dendrite arm, and the concentration of the intergranular composition in the three RHEAs. The

average composition in each alloy was slightly different from the nominal composition. This was probably caused by the volatilization and splashing of the alloy during melting and related to error during the measurement. According to the qualitative examination of the backscattered electron imaging (BEI) SEM pictures, the element distribution in the as-cast alloys was inhomogeneous. Dendrite arms are abundant in heavy metals with higher melting temperatures (Ta and Nb). Heavy metals with relatively high melting points (Ta and Nb) were abundant in dendritic arms. On the contrary, light elements were concentrated in the interdendrites (Zr) or distributed uniformly in the alloy (Ti and V). Similar phenomena have been found in other RHEAs [16].

Table 1. The estimated bulk composition (C_{aver}), the average composition of dendrite arms (C_{dr}), and the average composition of interdendritic regions (C_{idr}) for $(TiZr)_x(NbTaV)_{1-x}$ HEAs. The yield strengths ($\sigma_{0.2}$) of pure metals are also given [16].

Alloys	Concentrations (at.%)	Ti	Zr	Nb	Ta	V
$(TiZr)_{0.4}(NbTaV)_{0.6}$	C_{aver}	24.3	26.3	16.6	18.5	14.3
	C_{dr}	26.7	23	16.7	19.8	13.9
	C_{idr}	26.3	35.2	11.9	12.6	14
$(TiZr)_{0.6}(NbTaV)_{0.4}$	C_{aver}	28.3	28.8	15.1	13.5	14.4
	C_{dr}	29.1	25.3	18.4	13.8	13.5
	C_{idr}	28.8	33.2	12.3	11.3	14.5
$(TiZr)_{0.8}(NbTaV)_{0.2}$	C_{aver}	35.7	34.8	11.6	9.2	8.8
	C_{dr}	36.4	31.4	14.2	9.5	7.5
	C_{idr}	35.2	40.2	8.8	6.9	8.9
$\sigma_{0.2}$ (MPa)		195	280	240	345	310

3.3. Formatting of Mathematical Components

The engineering stress–strain (σ – ϵ) curves upon compression at room temperature for as-cast $(TiZr)_x(NbTaV)_{1-x}$ HEAs ($x = 0.4, 0.6,$ and 0.8) in this study are depicted in Figure 4. As can be seen in Figure 4, all three alloys had good strength and plasticity and exhibited work hardening. Table 2 provides the data on the engineering yield strength and compressive strain. The maximum error was less than 50 MPa and 2% for yield strength and failure strain, respectively.

Table 2. The engineering yield stress and strain data for both compressive and tensile data of $(TiZr)_x(NbTaV)_{1-x}$ HEAs.

Alloys	TiZrNbTaV	$(TiZr)_{0.6}(NbTaV)_{0.4}$	$(TiZr)_{0.8}(NbTaV)_{0.2}$	$(TiZr)_{0.8}(NbTaV)_{0.2}$ (Tensile)
$\sigma_{0.2}$ (MPa)	1162	878	845	847, 934 (cold rolling)
ϵ_p ,%	15.5	28.7	>50	8.5, 12.6 (cold rolling)

In order to better discuss the mechanical properties of the alloys, we converted the engineering stress–strain curve into a true stress–strain curve, as shown in Figure 5. The yield strength and maximum compressive fracture strength for the $(TiZr)_{0.4}(NbTaV)_{0.6}$ alloy were 1300 and 1500 MPa, respectively, and its compressive strain was 13.5% before fracture. The stress–strain curves from the compression experiments on this alloy were not smooth. This may be related to the casting pores caused by the large melting point difference between the constituted elements of the alloy. For the $(TiZr)_{0.6}(NbTaV)_{0.4}$ RHEA, the yield strength was decreased to 900 MPa but exhibited about 30% compressive strain before fracture. Clearly, the $(TiZr)_{0.8}(NbTaV)_{0.2}$ alloy had significantly improved plasticity and slightly decreased yield strength compared with the $(TiZr)_{0.6}(NbTaV)_{0.4}$ alloy, which had a compressive strength and strain of 1180 MPa and 50%.

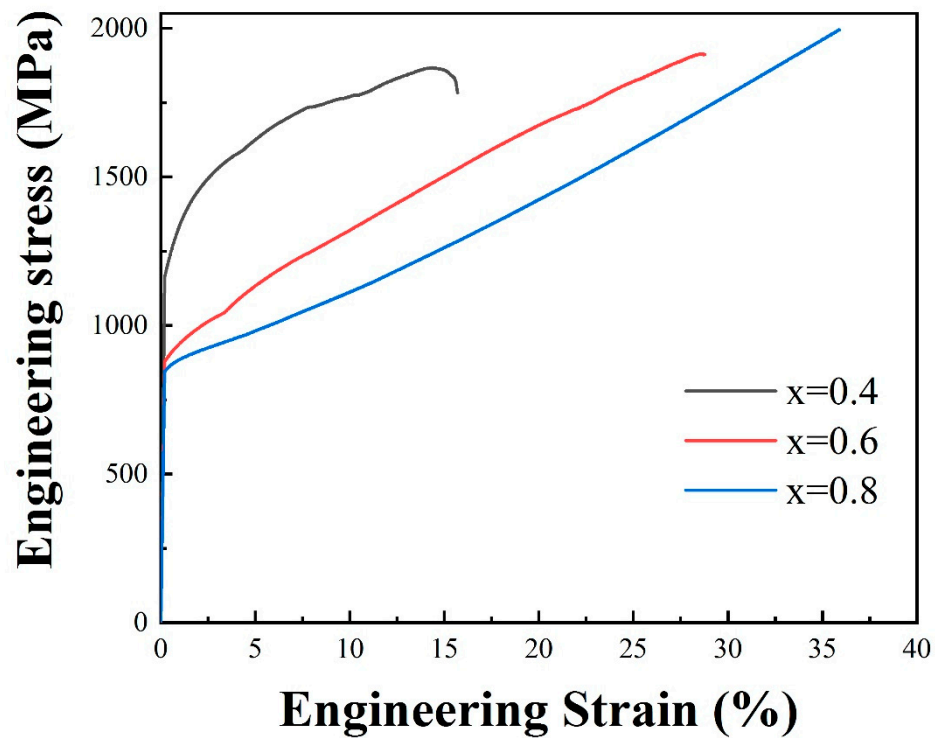


Figure 4. Compressive engineering stress–strain curves for $(\text{TiZr})_x(\text{NbTaV})_{1-x}$ ($x = 0.4, 0.6,$ and 0.8) RHEAs at room temperature.

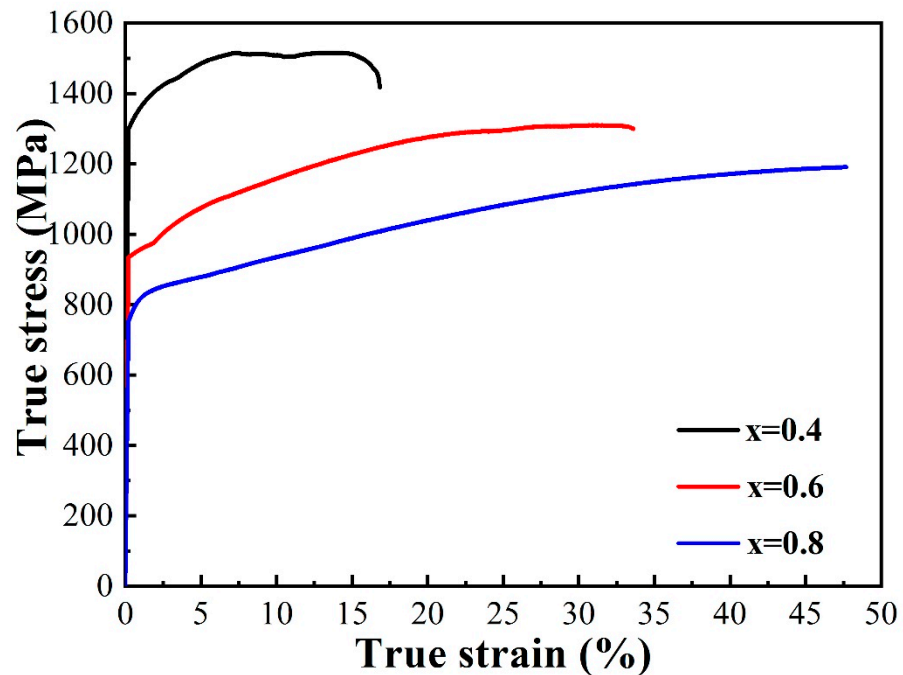


Figure 5. Compressive true stress–strain curves for $(\text{TiZr})_x(\text{NbTaV})_{1-x}$ ($x = 0.4, 0.6,$ and 0.8) RHEAs at room temperature.

Figure 6 depicts the yield strength and plasticity obtained upon compression at room temperature for some reported RHEAs [17–34]. Most of these alloys can be divided into two groups: (i) strong but brittle alloys which have a high yield strength of ≥ 1000 MPa and plasticity of $\leq 20\%$, and (ii) ductile but soft alloys, which have a yield strength of < 1200 MPa and plasticity of more than 50%. The three RHEAs in this work are also included in this

figure. Remarkably, the $(\text{TiZr})_{0.4}(\text{NbTaV})_{0.6}$ RHEA is located in a high-strength region in this figure, where most refractory alloys are located. The alloy has extraordinarily high strength, equivalent to that of some alloys containing W and Mo components, and good tensile ductility. The alloy $(\text{TiZr})_{0.6}(\text{NbTaV})_{0.4}$ offers several benefits, including high strength and an outstanding strength–ductility balance. The plasticity of $(\text{TiZr})_{0.8}(\text{NbTaV})_{0.2}$ is better than 50%, but the strength is lower, with a value of 800 MPa. Most refractory alloys in this region have obvious room temperature tensile ductility, and this means that it is possible to obtain tensile ductility for the $(\text{TiZr})_{0.8}(\text{NbTaV})_{0.2}$ alloy at room temperature.

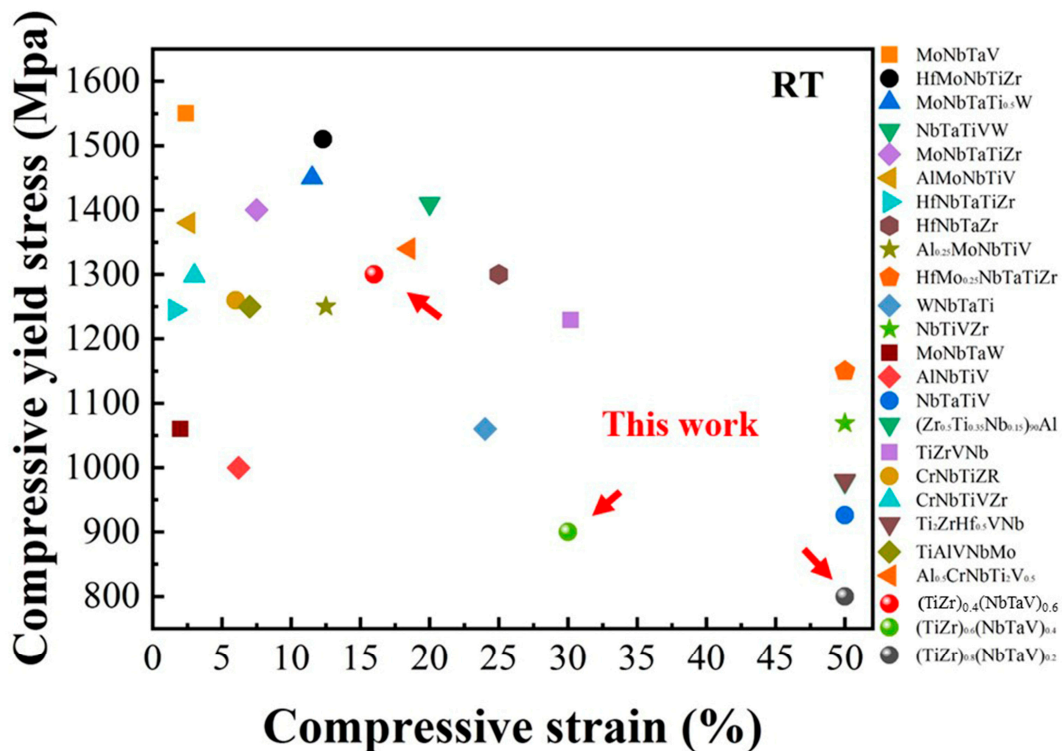


Figure 6. Compressive yield strength and plasticity of $(\text{TiZr})_x(\text{NbTaV})_{1-x}$ RHEAs and some reported RHEAs at room temperature.

Because of the impressive compressive plasticity, further tensile experiments for the $(\text{TiZr})_{0.8}(\text{NbTaV})_{0.2}$ alloy were carried out. In order to better display the tensile properties of the alloy, the engineering and true stress–strain (σ – ϵ) tensile curves for the $(\text{TiZr})_{0.8}(\text{NbTaV})_{0.2}$ alloy at room temperature are presented in Figures 7 and 8. From true stress–strain (σ – ϵ) tensile curves, the yield strength and plastic strains for the as-cast samples were 850 MPa and 7%, and the samples under cold rolling (20% reduction) showed higher yield strength (950 MPa) and plastic fracture strain (10%). These results show that the alloy has good tensile plasticity and strength at room temperature. The performance improvement after cold rolling may be related to the reduction in casting defects.

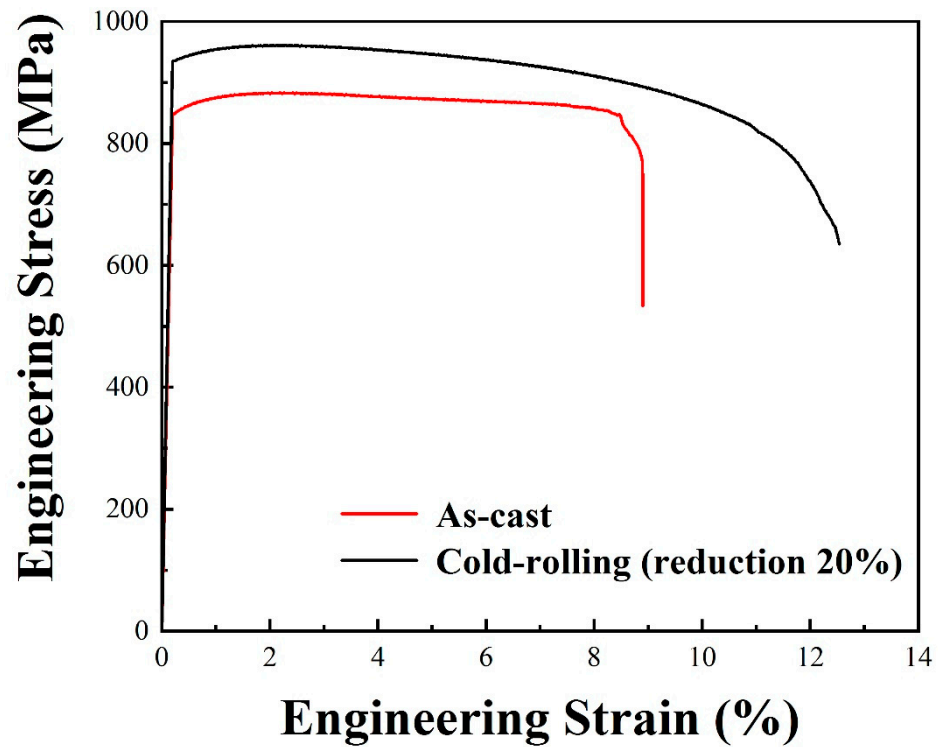


Figure 7. Tensile engineering stress–strain curves for the $(\text{TiZr})_{0.8}(\text{NbTaV})_{0.2}$ RHEA at room temperature.

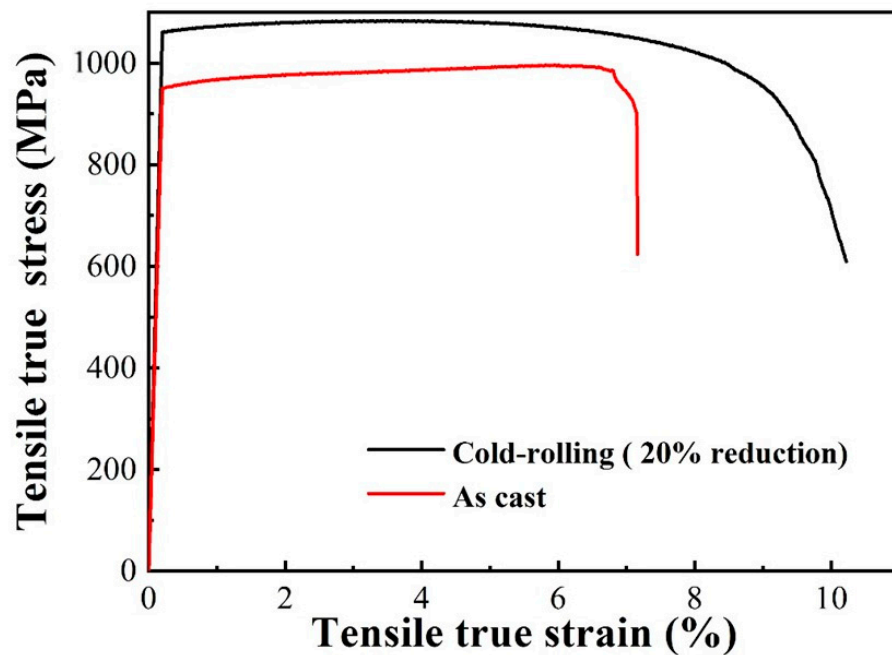


Figure 8. Tensile true stress–strain curves for the $(\text{TiZr})_{0.8}(\text{NbTaV})_{0.2}$ RHEA at room temperature.

4. Discussion

4.1. Phase Formation Rule

In traditional thermodynamics, it is generally believed that alloys containing a variety of major elements will form complex and brittle intermetallic compounds. By contrast, multicomponent HEAs promote the formation of simple solid solutions and inhibit the generation of intermetallic compounds due to their high configurational entropy. During HEA solidification, due to element segregation, disordered–ordered transformation, and

amplitude modulation decomposition, the actual configuration entropy of multicomponent alloys is lower than the ideal value. In this case, although the ideal configuration entropy of the alloys is high, the formation of intermetallic compounds is not totally inhibited [35]. As a result, various semi-empirical factors have been used to forecast phase development in the current HEAs. These parameters include the thermodynamic variable, which is defined on the basis of the entropy–enthalpy competition notion, Ω [36]; the atomic size difference, δ [37]; electronegativity, $\Delta\chi_{\text{Allen}}$ [38]; and valence electron concentration, VEC [39]. Of these parameters, the atomic size difference δ and the thermodynamic variable Ω are the most critical factors in deciding whether a solid solution will form. δ and Ω can be written as:

$$\delta = 100\% \sqrt{\sum_{i=1}^n c_i \left(1 - r_i / \sum_{j=1}^n c_j r_j\right)} \quad (3)$$

where r_i and r_j are the atomic radii of elements i and j , respectively, and c_i and c_j represent the atomic fractions of element i and element j , respectively.

$$\Omega = T\Delta S_{\text{mix}} / |\Delta H_{\text{mix}}| \quad (4)$$

where T denotes the melting point of an n -element alloy, ΔS_{mix} is the mixing entropy, and ΔH_{mix} is the enthalpy of mixing. According to the reported literature, a rule for solid-solution formation in multi-component HEAs is $\Omega \geq 1.1$ and $\delta \leq 6.6\%$ [36].

In addition, according to the Hume-Rothery rule, electronegativity has a major impact on phase formation in HEAs, and the following expression can be used:

$$\Delta\chi = \sqrt{\sum_{i=1}^n c_i (\chi_i - \bar{\chi})^2} \quad (5)$$

where χ_i is the electronegativity of element i and $\bar{\chi}$ is the average electronegativity of the elements in the alloys. Solid solutions are simple to form when the electronegativity is low.

The above three parameters can effectively determine the formation of the solid solution phase, but the specific crystal structure of the HEAs cannot be predicted. Later, Guo et al. [39] proposed the VEC theory to solve this problem:

$$\text{VEC} = \sum_{i=1}^n c_i (\text{VEC}_i) \quad (6)$$

where VEC_i is the VEC of the i th element. The theory holds that a single FCC phase is formed when $\text{VEC} > 8.0$, a single BCC phase is formed when $\text{VEC} < 6.87$, and both phases coexist when the value is between them. However, the criterion for the HCP phase was not clear at first. Recently, Yuan's work initially solved this problem: a single HCP or BCC phase was formed when $\text{VEC} < 4.09$ and $\text{VEC} > 4.18$, respectively, and the mixed HCP and BCC phases were formed in between [40].

The validity of these parameters in the current alloy system was testified, as calculated and listed in Table 3. With them, it was predicted to form a single-phase BCC solid solution in $(\text{TiZr})_x(\text{NbTaV})_{1-x}$ alloys, but this was not entirely consistent with the experimental results. For example, the calculated VEC value for the $(\text{TiZr})_{0.8}(\text{NbTaV})_{0.2}$ RHEA was 4.2, which was higher than the proposed threshold value of 4.18. This indicates that HCP and BCC can coexist when $\text{VEC} = 4.2$.

Table 3. The atomic radius (δ), enthalpy of mixing (ΔH_{mix}), entropy of mixing (ΔS_{mix}), melting temperature (T_m), Ω parameter, electronegativity difference ($\Delta\chi$), and valence electron concentration (VEC) of as-cast $(\text{TiZr})_x(\text{NbTaV})_{1-x}$ HEAs.

Alloys	Δ [%]	ΔH_{mix} [kJ/mol]	ΔS_{mix} [J/K/mol]	T_m [K]	Ω	$\Delta\chi$	VEC
$(\text{TiZr})_{0.4}(\text{NbTaV})_{0.6}$	6.35	0.32	13.38	2458	102.8	7.5	4.6
$(\text{TiZr})_{0.6}(\text{NbTaV})_{0.4}$	6.32	0.50	12.67	2286	57.9	7.5	4.35
$(\text{TiZr})_{0.8}(\text{NbTaV})_{0.2}$	5.87	0.41	10.71	2181	58.4	7.3	4.2

4.2. Solid Solution Strengthening

In the compression test at room temperature, the yield strength of the alloys was inversely proportional to the content of TiZr. In general, the influence of elements themselves can be judged by the rule of mixing (RoM):

$$p = \sum_{i=1}^n c_i p_i, \quad (7)$$

where c_i is the atomic fraction of the i th element, p is the yield strength of the alloy, and p_i is the mechanical property of element i (provided in Table 1). The calculated averages $\sigma_{0.2}^{mix}$ of the $(\text{TiZr})_x(\text{NbTaV})_{1-x}$ alloys are listed in Table 4. According to the calculation by RoM, there was little difference in theoretical yield strength between the three alloys. The calculated value was much less than the measured yield strength, which indicates that some other strengthening mechanisms exist in the alloys. The change in the alloy strength was affected little by the element itself and was highly dependent on the strengthening mode caused by the change in element content.

Table 4. Comparison between the calculated yield strength and the experimental value; the values by rule of mixing and compressive strain are also listed.

Alloys	$\sigma_{0.2}$ (MPa)		Exp.	Cal.	Exp/Cal	ε_p , %
	RoM					
$(\text{TiZr})_{0.4}(\text{NbTaV})_{0.6}$	274		1315	1515	0.87	17
$(\text{TiZr})_{0.6}(\text{NbTaV})_{0.4}$	259		950	1240	0.77	35
$(\text{TiZr})_{0.8}(\text{NbTaV})_{0.2}$	250		786	1187	0.66	>50

Considering the compositional complexity in HEAs, solid solution strengthening (SSS) is projected to have a significant impact. The elastic interactions between dislocation local stress fields and solute atoms cause SSS in metallic solid solutions [41,42]. The interaction force, F , is mainly provided by two sources, i.e., the atomic size misfit parameter, $\delta_a = (1/a)da/dc$, and the modulus misfit parameter, $\delta_\mu = (1/\mu)d\mu/dc$, of the solute and solvent elements.

$$F = \mu b^2 \delta = \mu b^2 (\delta_\mu + \beta \delta_a), \quad (8)$$

In this equation, μ is the alloy's shear modulus, b is the magnitude of the Burgers vector, a is the lattice parameter, c is the solute atom fraction, and β is a constant whose value changes according to the kind of movable dislocation. Screw dislocations are often assigned a value of 4. On the other hand, $\beta \geq 16$ is used for edge dislocations. The value of β was set to 9 because the common dislocation type in most alloys is a random blend of edge and screw dislocations [43].

The solute-induced stress increases in a concentrated solid solution, $\Delta\sigma$, can be defined as:

$$\Delta\sigma = Zb^{-2}F^{4/3}c^{2/3}E_L^{-1/3}, \quad (9)$$

where Z is a material constant with no dimensions, which is of the order of 0.1; c is the solute concentration; and E_L is the dislocation line tension, which is typically expressed as

$E_L = \mu b^2$. Using Equations (8) and (9), the value for the SSS caused by the i th element can be calculated from:

$$\Delta\sigma_i = AGf_i^{4/3}c_i^{2/3}, \quad (10)$$

where A is a material-dependent dimensionless constant of the order of 0.04 [16], and the f_i parameter can be calculated as follows:

$$f_i = \sqrt[2]{\delta_{\mu i}^2 + \beta^2 \delta_{ai}^2} \quad (11)$$

For the BCC-structured single-phase HEAs, the δ_{ai} and $\delta_{\mu i}$ (per atom pair) in the vicinity of i th element can be calculated as the average difference of the atomic size δ_{aij} and the atomic modulus $\delta_{\mu ij}$ with its neighbor [43]:

$$\delta_{ai} = \frac{9}{8} \sum c_j \delta_{aij}, \quad (12)$$

$$\delta_{\mu i} = \frac{9}{8} \sum c_j \delta_{\mu ij}, \quad (13)$$

where c_j is the atomic fraction of the alloy's j th element, $\delta_{aij} = (a_i - a_j)/(a_i + a_j)$ and $\delta_{\mu ij} = (\mu_i - \mu_j)/(\mu_i + \mu_j)$. The alloys' SSS is obtained by summation over $\Delta\sigma_i$ of each constituent via:

$$\Delta\sigma = \left(\sum \Delta\sigma_i^{3/2} \right)^{2/3}, \quad (14)$$

Then, it is possible to roughly estimate the HEAs' calculated yield strength:

$$\sigma_{0.2}^{cal} = \sigma_{0.2}^{mix} + \Delta\sigma, \quad (15)$$

The model-predicted values of $(\text{TiZr})_x(\text{NbTaV})_{1-x}$ alloys are listed in Table 4. The model successfully predicted the yield strength of the equal atomic ratio alloy, equal to 1515 MPa, which was slightly larger than the experimental value. However, for both the $(\text{TiZr})_{0.6}(\text{NbTaV})_{0.4}$ and $(\text{TiZr})_{0.8}(\text{NbTaV})_{0.2}$ alloys, the SSS model is not very suitable. Specifically, at $x = 0.8$, the model may not be applicable. The alloy $(\text{TiZr})_{0.8}(\text{NbTaV})_{0.2}$ contains two phases and may have other strengthening ways, which means that the SSS plays a small role in this alloy. The alloy $(\text{TiZr})_{0.6}(\text{NbTaV})_{0.4}$ exhibits a straightforward BCC phase with a classic dendritic structure. It also involves the contribution of various elements. This is because as the molar ratio of TiZr increases, the elemental segregation and microstructure heterogeneity of the alloys increase. In addition, this simple solid solution strengthening model does not take that into account.

5. Conclusions

On the basis of TiZrNbTaHf RHEAs, relatively inexpensive $(\text{TiZr})_x(\text{NbTaV})_{1-x}$ RHEAs were designed. XRD and SEM were used to study the microstructure. Mechanical characteristics were determined by performing compression and tensile tests at room temperature. The following conclusions can be drawn:

(1) As-cast $(\text{TiZr})_{0.4}(\text{NbTaV})_{0.6}$ and $(\text{TiZr})_{0.6}(\text{NbTaV})_{0.4}$ alloys have a single BCC phase. In addition, a mixture of HCP + BCC structure was confirmed in the as-cast $(\text{TiZr})_{0.8}(\text{NbTaV})_{0.2}$ alloy, which is rarely reported in refractory high entropy alloys.

(2) In the compression test, the $(\text{TiZr})_{0.4}(\text{NbTaV})_{0.6}$ RHEA had a yield strength of 1300 MPa with a fracture plastic strain of 16%. For $(\text{TiZr})_{0.6}(\text{NbTaV})_{0.4}$, the measured yield strength and compression fracture strain were 950 MPa and 35%. In addition, $(\text{TiZr})_{0.8}(\text{NbTaV})_{0.2}$ is an extremely ductile material that does not fracture until it reaches 50% strain. In tensile tests at room temperature, the alloy had a tensile plasticity of 7% and a yield strength of 800 MPa. New evidence was provided to solve the room temperature brittleness of refractory high entropy alloys.

(3) The simple SSS model accurately predicts the yield strength of $(\text{TiZr})_{0.4}(\text{NbTaV})_{0.6}$ but not $(\text{TiZr})_{0.6}(\text{NbTaV})_{0.4}$ or $(\text{TiZr})_{0.8}(\text{NbTaV})_{0.2}$ RHEAs. The forecast error of $(\text{TiZr})_{0.6}(\text{NbTaV})_{0.4}$ was not large, while $(\text{TiZr})_{0.8}(\text{NbTaV})_{0.2}$ had a large forecast error because it contains two phases. This model may be more suitable for a BCC alloy with a single equal atomic ratio.

Author Contributions: Conceptualization, Z.L. and J.Q.; Data curation, Z.L.; Formal analysis, Z.L.; Investigation, Z.L. and X.S.; Methodology, Z.L.; Project administration, J.Q.; Supervision, J.Q.; Validation, Z.L. and J.Q.; Visualization, M.Z.; Writing—original draft, Z.L.; Writing—review and editing, X.S., M.Z., and J.Q. All authors have read and agreed to the published version of the manuscript.

Funding: This research was funded by the National Natural Science Foundation of China (No. 52271110), the Fundamental Research Program of Shanxi Province, China (No. 202203021211130), and the State Key Lab of Advanced Metals and Materials (No.2022-Z22).

Data Availability Statement: The data that support the findings of this study are available from the corresponding author upon reasonable request.

Acknowledgments: The authors would like to acknowledge the financial support of the National Natural Science Foundation of China (No. 52271110), the Fundamental Research Program of Shanxi Province, China (No. 202203021211130), and the State Key Lab of Advanced Metals and Materials (No.2022-Z22).

Conflicts of Interest: The authors have no conflict to disclose.

References

1. Ritchie, R.O. The conflicts between strength and toughness. *Nat. Mater.* **2011**, *10*, 817–822. [[CrossRef](#)] [[PubMed](#)]
2. Cantor, B.; Chang, I.T.H.; Knight, P.; Vincent, A.J.B. Microstructural development in equiatomic multicomponent alloys. *Mater. Sci. Eng. A* **2004**, *375–377*, 213–218. [[CrossRef](#)]
3. Yeh, J.W.; Chen, S.K.; Lin, S.J.; Gan, J.Y.; Chin, T.S.; Shun, T.T.; Tsau, C.H.; Chang, S.Y. Nanostructured high-entropy alloys with multiple principal elements: Novel alloy design concepts and outcomes. *Adv. Eng. Mater.* **2004**, *6*, 299–303. [[CrossRef](#)]
4. Zhang, W.; Liaw, P.K.; Zhang, Y. Science and technology in high-entropy alloys. *Sci. China Mater.* **2018**, *61*, 2. [[CrossRef](#)]
5. Senkov, O.; Wilks, G.; Miracle, D.; Chuang, C.; Liaw, P. Refractory high-entropy alloys. *Intermetallics* **2010**, *18*, 1758–1765. [[CrossRef](#)]
6. Qiao, J.W.; Bao, M.; Zhao, Y.; Yang, H.; Wu, Y.; Zhang, Y.; Hawk, J.; Gao, M.C. Rare-earth high entropy alloys with hexagonal close-packed structure. *J. Appl. Phys.* **2018**, *124*, 195101. [[CrossRef](#)]
7. Yao, J.Q.; Liu, X.W.; Gao, N.; Jiang, Q.H.; Li, N.; Liu, G.; Zhang, W.B.; Fan, Z.T. Phase stability of a ductile single-phase BCC $\text{Hf}_{0.5}\text{Nb}_{0.5}\text{Ta}_{0.5}\text{Ti}_{1.5}\text{Zr}$ refractory high-entropy alloy. *Intermetallics* **2018**, *98*, 79–88. [[CrossRef](#)]
8. Gao, M.C.; Doğan, Ö.N.; King, P.; Rollett, A.D.; Widom, M. The first-principles design of ductile refractory alloys. *JOM* **2008**, *60*, 61–65. [[CrossRef](#)]
9. Xu, Z.Q.; Ma, Z.L.; Tan, Y.; Cheng, X.W. Designing TiVNbTaSi refractory high-entropy alloys with ambient tensile ductility. *Scr. Mater.* **2022**, *206*, 114230. [[CrossRef](#)]
10. Senkov, O.N.; Semiatin, S.L. Microstructure and properties of a refractory high-entropy alloy after cold working. *J. Alloys Compd.* **2015**, *649*, 1110–1123. [[CrossRef](#)]
11. Huang, H.; Wu, Y.; He, J.; Wang, H.; Liu, X.; An, K.; Wu, W.; Lu, Z. Phase-Transformation Ductilization of Brittle High-Entropy Alloys via Metastability Engineering. *Adv. Mater.* **2017**, *29*, 1701678. [[CrossRef](#)] [[PubMed](#)]
12. Kimura, M.; Matsuda, A.; Nakajima, K. X-ray determination of the volume fraction of retained austenite in quenched carbon steels. *J. Phys. D Appl. Phys.* **1973**, *6*, 21. [[CrossRef](#)]
13. Lowe-Ma, C.K.; Donlon, W.T.; Dowling, W.E. Comments on determining X-ray diffraction-based volume fractions of retained austenite in steels. *Powder Diffr.* **2012**, *16*, 198–204. [[CrossRef](#)]
14. Yao, H.W.; Qiao, J.W.; Gao, M.C.; Hawk, J.A.; Ma, S.G.; Zhou, H.F.; Zhang, Y. NbTaV-(Ti,W) refractory high-entropy alloys: Experiments and modeling. *Mater. Sci. Eng. A* **2016**, *674*, 203–211. [[CrossRef](#)]
15. Tu, C.-H.; Wu, S.-K.; Lin, C. A study on severely cold-rolled and intermediate temperature aged HfNbTiZr refractory high-entropy alloy. *Intermetallics* **2020**, *126*, 106935. [[CrossRef](#)]
16. Yao, H.W.; Qiao, J.W.; Hawk, J.A.; Zhou, H.F.; Chen, M.W.; Gao, M.C. Mechanical properties of refractory high-entropy alloys: Experiments and modeling. *J. Alloys Compd.* **2017**, *696*, 1139–1150. [[CrossRef](#)]
17. Juan, C.-C.; Tseng, K.-K.; Hsu, W.-L.; Tsai, M.-H.; Tsai, C.-W.; Lin, C.-M.; Chen, S.-K.; Lin, S.-J.; Yeh, J.-W. Solution strengthening of ductile refractory HfMoxNbTaTiZr high-entropy alloys. *Mater. Lett.* **2016**, *175*, 284–287. [[CrossRef](#)]
18. Coury, F.G.; Kaufman, M.; Clarke, A.J. Solid-solution strengthening in refractory high entropy alloys. *Acta Mater.* **2019**, *175*, 66–81. [[CrossRef](#)]

19. Juan, C.-C.; Tsai, M.-H.; Tsai, C.-W.; Lin, C.-M.; Wang, W.-R.; Yang, C.-C.; Chen, S.-K.; Lin, S.-J.; Yeh, J.-W. Enhanced mechanical properties of HfMoTaTiZr and HfMoNbTaTiZr refractory high-entropy alloys. *Intermetallics* **2015**, *62*, 76–83. [[CrossRef](#)]
20. Han, Z.; Chen, N.; Zhao, S.; Fan, L.; Yang, G.; Shao, Y.; Yao, K. Effect of Ti additions on mechanical properties of NbMoTaW and VNbMoTaW refractory high entropy alloys. *Intermetallics* **2017**, *84*, 153–157. [[CrossRef](#)]
21. Yao, H.; Qiao, J.-W.; Gao, M.C.; Hawk, J.A.; Ma, S.-G.; Zhou, H. Correction to Yao, H.; Qiao, J.-W.; Gao, M.C.; Hawk, J.A.; Ma, S.-G.; Zhou, H. MoNbTaV Medium-Entropy Alloy. *Entropy* **2016**, *18*, 189. *Entropy* **2016**, *18*, 289. [[CrossRef](#)]
22. Han, Z.; Luan, H.; Liu, X.; Chen, N.; Li, X.; Shao, Y.; Yao, K. Microstructures and mechanical properties of Ti_xNbMoTaW refractory high-entropy alloys. *Mater. Sci. Eng. A* **2018**, *712*, 380–385. [[CrossRef](#)]
23. Wang, S.-P.; Xu, J. TiZrNbTaMo high-entropy alloy designed for orthopedic implants: As-cast microstructure and mechanical properties. *Mater. Sci. Eng. C* **2017**, *73*, 80–89. [[CrossRef](#)] [[PubMed](#)]
24. Chen, S.Y.; Yang, X.; Dahmen, K.A.; Liaw, P.K.; Zhang, Y. Microstructures and crackling noise of Al_xNbTiMoV high entropy alloys. *Entropy* **2014**, *16*, 870–884. [[CrossRef](#)]
25. Senkov, O.N.; Wilks, G.; Scott, J.; Miracle, D.B. Mechanical properties of Nb₂₅Mo₂₅Ta₂₅W₂₅ and V₂₀Nb₂₀Mo₂₀Ta₂₀W₂₀ refractory high entropy alloys. *Intermetallics* **2011**, *19*, 698–706. [[CrossRef](#)]
26. Yurchenko, N.Y.; Stepanov, N.; Zharebtsov, S.; Tikhonovsky, M.; Salishchev, G. Structure and mechanical properties of B2 ordered refractory AlNbTiVZr_x (x = 0–1.5) high-entropy alloys. *Mater. Sci. Eng. A* **2017**, *704*, 82–90. [[CrossRef](#)]
27. Maiti, S.; Steurer, W. Structural-disorder and its effect on mechanical properties in single-phase TaNbHfZr high-entropy alloy. *Acta Mater.* **2016**, *106*, 87–97. [[CrossRef](#)]
28. Senkov, O.N.; Senkova, S.V.; Woodward, C.; Miracle, D.B. Low-density, refractory multi-principal element alloys of the Cr–Nb–Ti–V–Zr system: Microstructure and phase analysis. *Acta Mater.* **2013**, *61*, 1545–1557. [[CrossRef](#)]
29. Yan, X.; Liaw, P.K.; Zhang, Y. Ultrastrong and ductile BCC high-entropy alloys with low-density via dislocation regulation and nanoprecipitates. *J. Mater. Sci. Technol.* **2022**, *110*, 109–116. [[CrossRef](#)]
30. Huang, T.-D.; Wu, S.-Y.; Jiang, H.; Lu, Y.-P.; Wang, T.-M.; Li, T.-J. Effect of Ti content on microstructure and properties of Ti_xZrVNb refractory high-entropy alloys. *Int. J. Miner. Metall. Mater.* **2020**, *27*, 1318–1325. [[CrossRef](#)]
31. Senkov, O.N.; Senkova, S.V.; Miracle, D.B.; Woodward, C. Mechanical properties of low-density, refractory multi-principal element alloys of the Cr–Nb–Ti–V–Zr system. *Mater. Sci. Eng. A* **2013**, *565*, 51–62. [[CrossRef](#)]
32. Qiao, D.-X.; Jiang, H.; Jiao, W.-N.; Lu, Y.-P.; Cao, Z.-Q.; Li, T.-J. A novel series of refractory high-entropy alloys Ti₂ZrHf_{0.5}VNb_x with high specific yield strength and good ductility. *Acta Metall. Sin. (Engl. Lett.)* **2019**, *32*, 925–931. [[CrossRef](#)]
33. Xu, Z.Q.; Ma, Z.L.; Wang, M.; Chen, Y.W.; Tan, Y.D.; Cheng, X.W. Design of novel low-density refractory high entropy alloys for high-temperature applications. *Mater. Sci. Eng. A* **2019**, *755*, 318–322. [[CrossRef](#)]
34. Stepanov, N.D.; Yurchenko, N.Y.; Panina, E.S.; Tikhonovsky, M.A.; Zharebtsov, S.V. Precipitation-strengthened refractory Al_{0.5}CrNbTi₂V_{0.5} high entropy alloy. *Mater. Lett.* **2017**, *188*, 162–164. [[CrossRef](#)]
35. Ye, Y.; Wang, Q.; Lu, J.; Liu, C.; Yang, Y. High-entropy alloy: Challenges and prospects. *Mater. Today* **2016**, *19*, 349–362. [[CrossRef](#)]
36. Zhang, Y.; Lu, Z.; Ma, S.; Liaw, P.; Tang, Z.; Cheng, Y.; Gao, M. Guidelines in predicting phase formation of high-entropy alloys. *MRS Commun.* **2014**, *4*, 57–62. [[CrossRef](#)]
37. Zhang, Y.; Zhou, Y.J.; Lin, J.P.; Chen, G.L.; Liaw, P.K. Solid-solution phase formation rules for multi-component alloys. *Adv. Eng. Mater.* **2008**, *10*, 534–538. [[CrossRef](#)]
38. Poletti, M.G.; Battezzati, L. Electronic and thermodynamic criteria for the occurrence of high entropy alloys in metallic systems. *Acta Mater.* **2014**, *75*, 297–306. [[CrossRef](#)]
39. Guo, S.; Ng, C.; Lu, J.; Liu, C. Effect of valence electron concentration on stability of fcc or bcc phase in high entropy alloys. *J. Appl. Phys.* **2011**, *109*, 103505. [[CrossRef](#)]
40. Yuan, Y.; Wu, Y.; Yang, Z.; Liang, X.; Lei, Z.; Huang, H.; Wang, H.; Liu, X.; An, K.; Wu, W. Formation, structure and properties of biocompatible TiZrHfNbTa high-entropy alloys. *Mater. Res. Lett.* **2019**, *7*, 225–231. [[CrossRef](#)]
41. Labusch, R. A statistical theory of solid solution hardening. *Phys. Status Solidi B* **1970**, *41*, 659–669. [[CrossRef](#)]
42. Fleischer, R.L. Substitutional solution hardening. *Acta Metall.* **1963**, *11*, 203–209. [[CrossRef](#)]
43. Senkov, O.; Scott, J.; Senkova, S.; Miracle, D.; Woodward, C. Microstructure and room temperature properties of a high-entropy TaNbHfZrTi alloy. *J. Alloys Compd.* **2011**, *509*, 6043–6048. [[CrossRef](#)]

Disclaimer/Publisher’s Note: The statements, opinions and data contained in all publications are solely those of the individual author(s) and contributor(s) and not of MDPI and/or the editor(s). MDPI and/or the editor(s) disclaim responsibility for any injury to people or property resulting from any ideas, methods, instructions or products referred to in the content.